ELECTRONIC SEISMOLOGIST

Finite-Fault Rupture Detector (*FinDer*): Going Real-Time in Californian *ShakeAlert* Warning System

by M. Böse, C. Felizardo, and T. H. Heaton

INTRODUCTION

Rapid detection of local and regional earthquakes and issuance of fast alerts for impending shaking is considered beneficial to save lives, reduce losses, and shorten recovery times after destructive events (Allen *et al.*, 2009). Over the last two decades, several countries have built operational earthquake early warning (EEW) systems, including Japan (Hoshiba *et al.*, 2008), Mexico (Espinosa-Aranda *et al.*, 1995), Romania (Mărmureanu *et al.*, 2011), Turkey (Erdik *et al.*, 2003), Taiwan (Hsiao *et al.*, 2011), and China (Peng *et al.*, 2011). Other countries, such as the United States (Böse, Allen, *et al.*, 2013), Italy (Satriano *et al.*, 2011), and Switzerland (Behr *et al.*, 2015), are currently developing systems or evaluating algorithms in their seismic real-time networks.

Over the past eight years, scientists at the California Institute of Technology (Caltech), the University of California–Berkeley, the University of Southern California, the University of Washington, the U.S. Geological Survey (USGS), and the Swiss Federal Institute of Technology (ETH Zurich, Switzerland) developed the U.S. west-coast-wide *ShakeAlert* EEW demonstration system for California, Oregon, and Washington (Böse, Allen, *et al.*, 2013). Real-time alerts are currently being shared with around 300 individuals, companies, and emergency response organizations to gather feedback about system performance, to educate potential end users about EEW, and to identify needs and applications of a future operational warning system.

To quickly determine earthquake magnitudes and (point-source) hypocenter locations, the Californian *ShakeAlert* system processes and interprets real-time waveform data streams from several hundred seismic broadband velocity and strong-motion acceleration sensors as part of the California Integrated Seismic Network (CISN). Designed as a hybrid system, *ShakeAlert* combines the estimates from one single-sensor and two network-based EEW algorithms that run in parallel, including τ_c–P_d *Onsite* (Wu *et al.*, 2007; Böse, Hauksson, Solanki, Kanamori, Wu, *et al.*, 2009; Böse, Hauksson, Solanki, Kanamori, and Heaton, 2009), *ElarmS* (Allen, 2007; Kuyuk *et al.*, 2014), and the *Virtual Seismologist* (Cua *et al.*, 2009; Behr *et al.*, 2015). Once an earthquake has been detected, each algorithm starts independently sending reports to the *ShakeAlert* Decision Module, which—based on these reports—determines the most probable event parameters (location, magnitude, and origin time) and uncertainties, which are then continuously updated with progressing time as new data arrive. Using these estimated source parameters, the *ShakeAlert* UserDisplay software, which is installed at the end user's site and subscribes to the *ShakeAlert* system, predicts and displays the arrival and intensity of expected peak shaking (Böse, Allen, *et al.*, 2013).

Encouraged by its promising real-time performance during the recent moderate-size 2014 **M** 5.1 La Habra and **M** 6.0 South Napa earthquakes in southern and northern California, the *ShakeAlert* Science team decided in 2014 to include the Finite-fault rupture Detector algorithm, *FinDer* (Böse *et al.*, 2012), as a fourth seismic algorithm in the *ShakeAlert* system to enable the use of rupture-to-site distances in ground-motion predictions and hence improve EEW performance during large-magnitude (**M** ≥ 6.0) earthquakes. Based on a rapid near- or far-source classification and comparison with precalculated templates, *FinDer* provides rapid estimates of the centroid position ($\mathrm{lat}_{\mathrm{centroid}}$, $\mathrm{lon}_{\mathrm{centroid}}$), length L, and strike Θ of an ongoing fault rupture, assuming a line source (Fig. 1). The integration of *FinDer* into *ShakeAlert* was finalized in April 2015. Currently, *FinDer* is operated as a MathWorks MATLAB (www.mathworks.com/products/matlab, last accessed September 2015) stand-alone code with a C++ waveform-processing module installed at three CISN datacenters at Caltech/USGS-Pasadena, UC Berkeley, and USGS-Menlo Park. Translation of the *FinDer* algorithm to C++ by USGS-Menlo Park, ETH Zurich, and Caltech is currently under way.

We will start this article with a brief review of the *FinDer* algorithm developed by Böse *et al.* (2012), followed by a summary and demonstration of recent improvements to the algorithm, including error estimates, usage of generic and fault-specific templates, and extension to subduction-zone earthquakes. We will demonstrate and evaluate the real-time and off-line performance of *FinDer* during the recent 2014 **M** 5.1 La Habra and **M** 6.0 South Napa (California) earthquakes, as well as the 2010 **M** 7.2 El Mayor–Cucapah (Mexico) and 2011 **M** 9.0 Tohoku-Oki (Japan) earthquakes.

REVIEW AND EXTENSION OF THE *FinDer* ALGORITHM

The *FinDer* algorithm uses image-recognition techniques to detect and model finite-fault ruptures using spatial images of observed ground motions and theoretical templates modeled from empirical ground-motion prediction equations (GMPEs).

 doi: 10.1785/0220150154

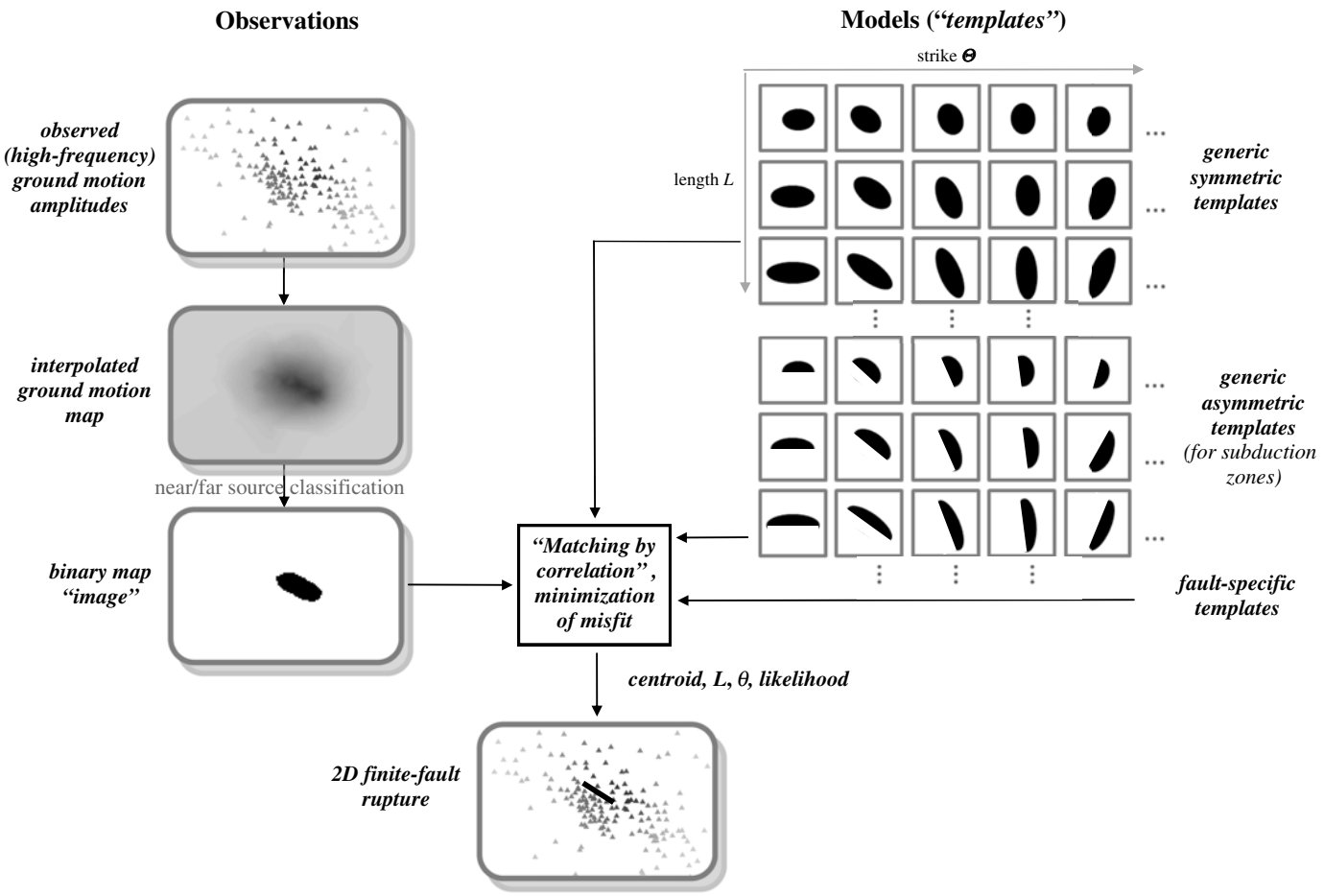

▲ **Figure 1.** Scheme of *FinDer* algorithm. Processing involves three steps: (1) near- or far-source classification of spatially interpolated high-frequency observations, which gives a binary image (left); (2) application of matching by correlation to determine the spatial correlation of the image and a template (right) for a given rupture length L and strike Θ; the location of maximum correlation gives the rupture centroid. Templates are generated from ground-motion prediction equations (GMPEs). Currently, we use three sets of templates (right): generic symmetric, generic asymmetric (for subduction zones), and fault specific; (3) minimization of the misfit between image and templates gives L, Θ, centroid, and likelihood $\mathcal{L}$ of the assumed line source. Estimates are updated regularly as new data become available (e.g., every second).

As described by Böse *et al.* (2012) and illustrated in Figure 1, *FinDer* processing involves three main steps: (1) near- or far-source classification of spatially interpolated high-frequency observations, which gives a binary image $I(x, y)$; (2) application of matching by correlation (e.g., Gonzales *et al.*, 2004) to determine the correlation $R(x, y|L, \Theta)$ of template $T(x, y|L, \Theta)$ and $I(x, y)$ at any spatial location (x, y); the geographic coordinates $\text{lat}_{\text{centroid}}$ and $\text{lon}_{\text{centroid}}$ of the rupture centroid come from the template spatial location that corresponds to the maximum spatial integral of the given template cross correlation with the data; (3) minimization of the misfit between image $I(x, y)$ and templates $T(x, y|L, \Theta)$ gives L, Θ, and $\text{lat}_{\text{centroid}}$ and $\text{lon}_{\text{centroid}}$ of the assumed line source. The output parameters are updated whenever a new set of ground-motion amplitudes becomes available (for instance, every second). This way, *FinDer* keeps track of a rupture evolving from a small point source to a large finite-rupture event.

Images $I(x, y)$ (Fig. 1, left) are obtained from map-projected and phase-independent (Böse *et al.*, 2012) interpolated logarithmic peak ground acceleration (PGA) amplitudes. We define PGA as the largest absolute value recorded on any of the three ground-motion components over a constant time window (e.g., 120 s), corresponding to the rupture duration of the largest expected earthquake in a given region. Because the large high-frequency motions are typically observed at only small rupture-to-site distances (e.g., Yamada *et al.*, 2007), a ground-motion threshold, *gm_threshold*, is applied for near- or far-source classification, where image pixels with $\text{PGA}_{\text{obs}} \geq gm\_threshold$ are set to 1 and otherwise are set to 0. For the examples shown in this article, we set $gm\_threshold = 70$ cm/s^2. We are using the term "near source" not in a strictly physical sense, but rather to characterize the spatial zone around the fault rupture with PGA values exceeding some arbitrary threshold.

Table 1
Description of Template Sets Used in This Study

	Generic Symmetric Templates	Fault-Specific Templates*	Generic Asymmetric Templates (Subduction Zones)
Range	L: 5–300 km, $\Delta L = 5$ km Θ: 0°–179°, $\Delta\Theta = 1°$	L: 15–350 km, $\Delta L = 5$ km Θ: follows fault-surface-trace of SAF for various rupture start and end positions, that is Θ is not fixed in a given template; three overlapping subsets such as southern SAF, middle SAF, and northern SAF	L: 10–450 km, $\Delta L = 10$ km Θ: 0–357°, $\Delta\Theta = 3°$
Size	77 × 77 cells (each cell: 5 × 5 km)	56 × 123 (southern SAF) 78 × 78 (middle SAF) 67 × 78 (northern SAF) (each cell: 5 × 5 km)	155 × 155 cells (each cell: 10 × 10 km)
Total number	10,800	1022 456 (southern SAF) 378 (middle SAF) 188 (northern SAF)	2700
GMPE†	Cua and Heaton (2009)	Cua and Heaton (2009)	Si and Midorikawa (2000)
L–**M** relation	Wells and Coppersmith (1994)	Wells and Coppersmith (1994)	Blaser *et al.* (2010)

*SAF, San Andreas fault.
†GMPE, ground-motion prediction equation.

Templates $T(x, y|L, \Theta)$ (Fig. 1, right) are precalculated binary images generated for various rupture lengths L and strikes Θ from empirical GMPEs, in which pixels close to the rupture ($PGA_{GMPE} \geq gm\_threshold$) are set to 1 and all other pixels ($PGA_{GMPE} < gm\_threshold$) to 0. The templates thus consist of equidistant buffer zones around the line source, bordered by two parallel lines and two semicircles, which result in quasi-elliptical shapes (Fig. 1, right). The relationship between the cutoff distance and the rupture length L (and thus magnitude **M**) is nonlinear due to the nonlinear nature of the underlying GMPEs for PGA, which saturate at large magnitudes and close distances.

Because of the assumed symmetry of the generic templates, the results of Θ and $\Theta + 180°$ are equivalent. It is assumed that near-source PGAs are not affected by rupture directivity, as discussed by Spudich and Chiou (2008). For the application of *FinDer* to earthquakes in California and northern Mexico as described in this article, we use GMPEs by Cua and Heaton (2009) and empirical rupture length–magnitude relations by Wells and Coppersmith (1994); for application to the Tohoku-Oki subduction-zone earthquake (Japan), we apply relations after Si and Midorawaka (2000) and Blaser *et al.* (2010).

Modeled templates $T(x, y|L, \Theta)$ are used as spatial filters to determine the correlation $R(x, y|L, \Theta)$ with an observed image $I(x, y)$ at each spatial location of T in I (the spatial extent of I is much larger than of T). This method is known as matching by correlation (e.g., Gonzales *et al.*, 2004; Fig. 1, middle). To increase computational speed, we implemented the algorithm in the Fourier domain by taking advantage of the correlation theorem:

$$I(x, y) \star T(x, y|L, \Theta) \Leftrightarrow \tilde{I}(k_x, k_y)\tilde{T}^*(k_x, k_y|L, \Theta), \quad (1)$$

which relates the spatial correlation to the product of the Fourier transforms $\tilde{I}(k_x, k_y)$ and $\tilde{T}^*(k_x, k_y|L, \Theta)$ in the wavenumber domain (k_x, k_y), in which the star denotes correlation and the asterisk denotes the complex conjugate. This approach is computationally highly efficient and could be easily parallelized for additional speed, though this has not been done yet in the current *FinDer* implementation (Böse *et al.*, 2012).

Although *FinDer* was originally developed for generic symmetric templates assuming simple line sources with symmetric quasi-elliptical ground-shaking distributions around the finite-fault rupture (Böse *et al.*, 2012), we recently added a new set of fault-specific templates to provide more accurate rupture estimates along curved fault segments, such as along the Big Bend section of the San Andreas fault (SAF) in southern California. In addition, we created a third set of generic asymmetric templates, particularly designed to meet the requirements of subduction-zone environments, where seismic observations are typically limited to the hanging wall side of the fault rupture (Fig. 1, right; shaded area corresponds to downward-dipping fault plane). Table 1 gives a summary of the three currently used sets of templates.

The finite-fault parameters (L, Θ, and centroid position) are determined in a two-step procedure. In the first step, matching by correlation is used to determine the optimum spatial position (x', y') of a given template T in image I. The position (x', y') refers to the lower left corner of the template, assuming that the origin $(0,0)$ of both T and I are in the lower

left corner. The rupture centroid position ($\mathrm{lat}_{\mathrm{centroid}}$, $\mathrm{lon}_{\mathrm{centroid}}$) is determined from the template midpoint at the position (x', y'). In the second step, we minimize the normalized sum of squared errors to find the optimum template and thus L and Θ. We modify the original error function defined in Böse *et al.* (2012) and define the new misfit E for a given image and a generic or fault-specific template for length L and strike Θ as

$$E(L,\Theta) = \frac{\sum_{x',y'} [I(x+x', y+y') - T(x', y'|L,\Theta)]^2}{\sum_{x',y'} \sigma_m^2(x', y')[I(x+x', y+y') + T(x', y'|L,\Theta)]}, \tag{2a}$$

in which the summation is done over $x' = 0 \ldots w-1$, $y' = 0 \ldots h-1$ for template dimensions $w \times h$. The weighting term $\sigma_m^2(x', y')$ in equation (2a) accounts for the model uncertainties of the GMPEs (σ_{GMPE}) used for template generation, which we define as

$$\sigma_m^2(x', y') = \begin{cases} (R - R_{\min})/(R_{gm\_threshold} - R_{\min}) + 1 & \text{if } R_{\min} \le R \le R_{gm\_threshold} \\ 2 - (R - R_{gm\_threshold})/(R_{\max} - R_{gm\_threshold}) & \text{if } R_{gm\_threshold} \le R \le R_{\max}, \\ 1 & \text{otherwise} \end{cases} \tag{2b}$$

in which $R_{gm\_threshold}$ is the rupture-to-cell distance at which $\mathrm{PGA}_{\mathrm{mean}} = gm\_threshold$ (e.g., $gm\_threshold = 70$ cm/s^2), $R_{\min}$ is the rupture-to-cell distance at which $\mathrm{PGA}_{\mathrm{mean}} - \sigma_{\mathrm{GMPE}} = gm\_threshold$, and $R_{\max}$ is the rupture-to-cell distance at which $\mathrm{PGA}_{\mathrm{mean}} + \sigma_{\mathrm{GMPE}} = gm\_threshold$. Equation (2b) describes a simple bilinear function that increases linearly from 1 to 2 for distances between $R_{\min}$ and R_{mean} and then decreases linearly back to 1 for distances between R_{mean} and $R_{\max}$. For distances smaller than $R_{\min}$ or larger than $R_{\max}$ $\sigma_m^2(x', y')$ is 1.

The template (and thus L and Θ) that shows the best agreement with image $I(x, y)$ is found through minimization of the misfit function in equation (2a), that is $E(L, \Theta) \rightarrow \min$. For the generic templates, we apply the simplex search algorithm by Lagarias *et al.* (1998) with upper and lower bounds for L and Θ, which is a direct search algorithm that does not require numerical or analytic gradients. The convergence rate toward the minimum is excellent and usually requires 30–50 iterations only. For fault-specific templates, we consider all possible templates (and thus all L) for a given region (northern, middle, and southern SAF; Table 1); and, for each of these templates, we determine E and the optimum solution. If its minimum misfit is smaller than for the generic templates (for a simple 1D line source), the fault-specific template is preferred, and otherwise we use the generic one. At the moment, we test both generic symmetric and fault-specific templates in California and asymmetric templates only in subduction-zone environments (Japan). In our current MATLAB implementation, the total optimization procedure takes ~1–2 s on an i686 @2826.177 MHz machine.

As a new feature of *FinDer*, we recently started to estimate uncertainties for the best solutions of rupture length $\tilde{L}$ and strike $\tilde{\Theta}$ by approximation of the multivariate likelihood function $\mathcal{L}$. For generic templates, we keep the centroid position and rupture length of the best solution ($\widetilde{\mathrm{lat}}_{\mathrm{centroid}}$, $\widetilde{\mathrm{lon}}_{\mathrm{centroid}}$, $\tilde{L}$) fixed and vary the strike Θ from 0° to 179° to determine the estimated univariate likelihood function for strike as

$$\mathcal{L}(\Theta|\tilde{L}, I(x,y)) = \frac{1}{\sigma_d\sqrt{2\pi}} e^{\frac{-0.5E}{\sigma_d^2}}. \tag{3}$$

Equation (3) is a probability density function that describes how well the predictions from a given set of model parameters (Θ, L)—and thus from a given template T—fit the observed data image I. The standard deviation σ_d describes the combined effects of assumed errors in the observations (including effects of interpolation) and the assumed prediction errors in the forward model, that is the GMPEs used for template generation. We experimented with various σ_d and found that $\sigma_d = 0.1$ gives reasonable results that are in good agreement with geodetic inversions (Minson, Murray, *et al.*, 2014).

In the next step, we keep the centroid position and strike of the best solution ($\widetilde{\mathrm{lat}}_{\mathrm{centroid}}$, $\widetilde{\mathrm{lon}}_{\mathrm{centroid}}$, $\tilde{\theta}$) fixed and walk through all L (5–300 km) to determine $\mathcal{L}(L|\tilde{\Theta}, I(x,y))$, similar to equation (3). For fault-specific templates, we determine the misfit for each template and thus for each L, and can easily apply equation (3) to calculate the likelihood function.

Although a simultaneous inversion of the likelihood functions for L, Θ, and the centroid position would be preferred, such computations are unrealistic under the strict time constraints in EEW. Also, assuming that L and Θ are largely uncorrelated appears valid for at least moderate-to-large earthquake ruptures.

FinDer PERFORMANCE

We will now demonstrate the performance of *FinDer* with the new features described above for four recent earthquakes. Three of them are crustal strike-slip, normal, and oblique faulting events that occurred recently in California (2014 **M** 5.1 La Habra and **M** 6.0 South Napa earthquakes) and in northern Mexico (2010 **M** 7.2 El Mayor–Cucapah); the fourth event is the 2011 **M** 9.0 Tohoku-Oki (Japan) subduction-zone earthquake. The latter is particularly challenging because station coverage is along one side of the fault rupture only. USGS *ShakeMaps* (Wald *et al.*, 1999) and finite-source solutions

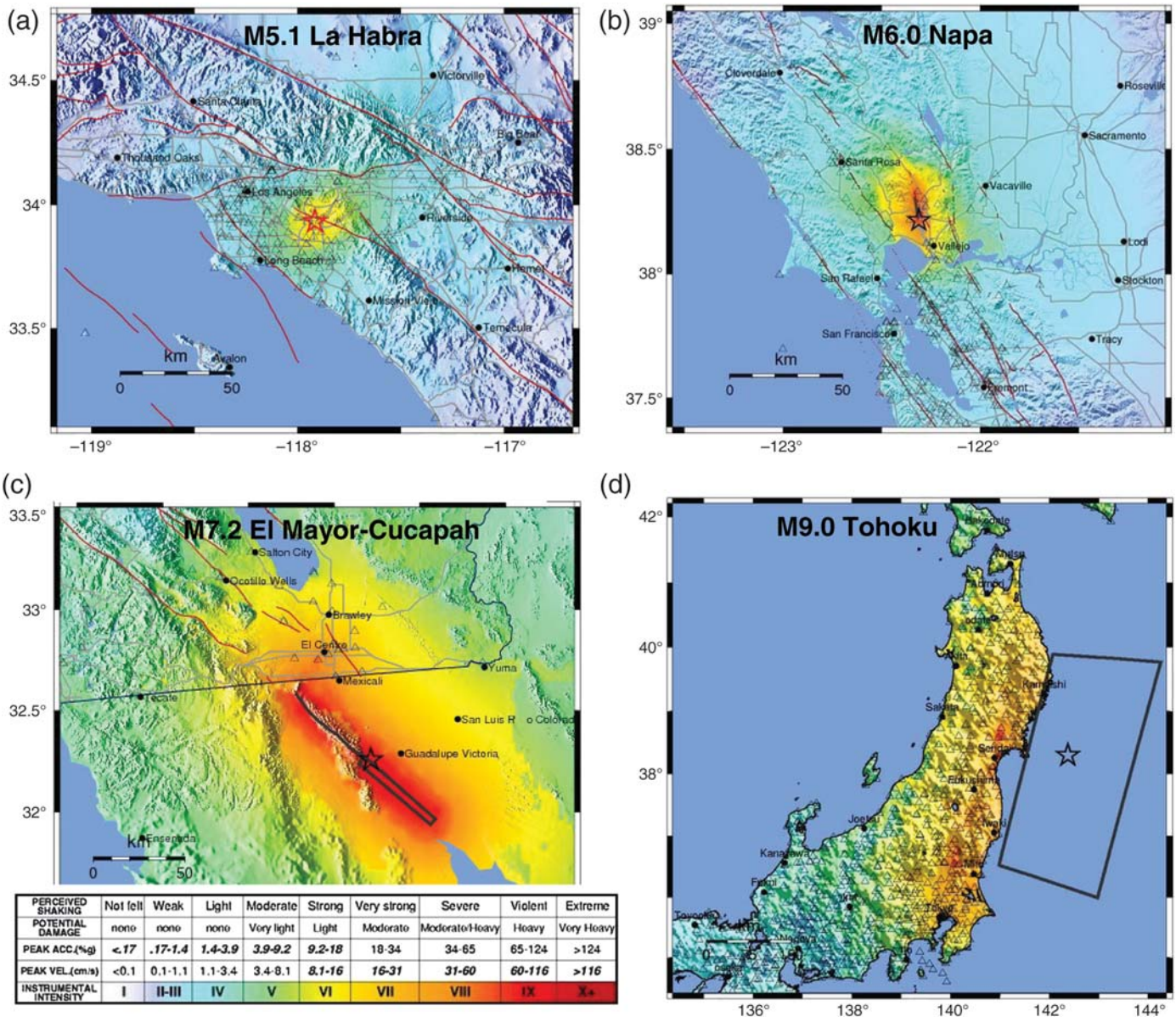

▲ **Figure 2.** U.S. Geological Survey (USGS) *ShakeMaps* showing the spatial distribution of observed instrumental intensities (modified Mercalli intensity [MMI]) in the (a) **M** 5.1 La Habra, (b) **M** 6.0 South Napa, (c) **M** 7.2 El Mayor–Cucapah, and (d) **M** 9.0 Tohoku-Oki earthquakes. Stars show epicenters, gray lines show 1D line source (b and c) or 2D rupture plane (c and d), respectively.

(Mai and Thingbaijam, 2014) for the four earthquakes are shown in Figure 2.

Real-Time Performance

The **M** 5.1 La Habra (California) earthquake on 28 March 2014 was felt widely throughout Orange, Los Angeles (LA), Ventura, Riverside, and San Bernardino Counties with a maximum observed instrumental intensity of VII close to the epicenter, located 1 km east of La Habra (Table 2). The Global Centroid Moment Tensor (Global CMT) moment tensor (see Data and Resources) shows oblique faulting, with a northward-dipping plane that approximately aligns with the Puente Hills thrust fault. The strike of the rupture is determined as $\Theta_{obs} = 232°$, which, due to symmetry in our 2D approach, is equivalent to $\Theta_{obs} = 52°$ (Table 2). The *ShakeAlert* EEW demonstration system detected the La Habra earthquake within 4.3 s of the event origin and provided 4 s of warning to Caltech in Pasadena, around 30 km from the epicenter (see Data and Resources).

During the La Habra earthquake, *FinDer* was running in real-time test mode at Caltech and getting waveform streams from 420 CISN strong-motion stations. However, *FinDer* was not connected to the *ShakeAlert* system. Although processing speed was not yet optimized, *FinDer* detected the earthquake within 11.5 s of the event origin and sent out a sequence of three internal reports with updated event information. The finite-fault solutions in these reports show an excellent agreement with the CMT solution (Table 2), as well as with the aftershock distribution of the La Habra earthquake ($L_{obs} \approx 10$ km; Fig. 3).

Table 2
Earthquake Source Parameters

Earthquake	Origin Time (UTC) (yyyy/mm/dd hh:mm:ss)	Hypocenter (latitude/longitude [°], depth [km])	Moment Magnitude (M)	Rupture Length L_{obs} (km)	Rupture Strike Θ_{obs} (°)
La Habra (oblique)	2014/03/29 04:09:42	33.932/−117.917, 4.8	5.1	10*	52†,‖
South Napa (strike slip)	2014/08/24 10:20:44	38.215/−122.312, 11.3	6.0	15–20*	157†,‖
El Mayor–Cucapah (complex)	2010/04/04 22:40:42	32.259/−115.287, 10	7.2 (starting as **M** ∼ 6.3‡)	120‡	132‡,‖
Tohoku-Oki (megathrust)	2011/03/11 05:46:23	38.297/142.272, 30	9.0	380§	202§

*Aftershock distribution.
†Global Centroid Moment Tensor (CMT) catalog (see Data and Resources).
‡Wei *et al.* (2011).
§Lay *et al.* (2011).
‖Because of our 2D approximation of the rupture, Θ_{obs} and $\Theta_{obs} - 180°$ are equivalent when using symmetric templates.

The 2014 **M** 6.0 South Napa earthquake on 24 August at 10:20:44 UTC occurred close to the West Napa fault. The Global CMT solution shows a strike-slip event with $\Theta_{obs} = 157°$; from the aftershock distribution and empirical relations by Wells and Coppersmith (1994), we estimate $L_{obs} \approx 15–20$ km. *ShakeAlert* detected this event within 5.1 s (Grapenthin *et al.*, 2014). The initial event location and moment magnitude were off by 3 km and 0.9 magnitude units (estimated magnitude was 5.1) compared with the Advanced National Seismic Network catalog. *FinDer*, again operating in real-time test mode but not connected to the *ShakeAlert* system, detected the event within 16 s. The fairly sparse distribution of strong-motion stations around the Napa earthquake led to larger uncertainties in the *FinDer*-estimated rupture strike, compared, for example, with the La Habra earthquake. Although the final strike estimate is off by around ∼30°–40°, the CMT solution of $\Theta_{obs} = 157°$ is within the *FinDer* real-time-estimated uncertainty range (Fig. 3).

Off-Line Performance

Following the La Habra and South Napa earthquakes, we started to improve the *FinDer* algorithm and code in terms of robustness and processing speed. To test our new implementation, we replayed archived waveforms from historic and simulated earthquakes using the *EarthWorm Tankplayer* software. In this article, we present the off-line-results from the La Habra and Napa earthquakes, as well as from the 2010 **M** 7.2 El Mayor–Cucapah and 2011 **M** 9.0 Tohoku earthquakes.

Figure 4 shows the *FinDer*-estimated rupture length L, strike Θ, and magnitude **M** for the four events. Magnitudes were estimated from empirical L–M relations by Wells and Coppersmith (1994) and Blaser *et al.* (2010). The shaded areas show the estimated uncertainties of the rupture parameters; they refer to the standard deviation estimated from the likelihood functions $\mathcal{L}$, assuming Gaussian distributions; if $\mathcal{L}$ is non-Gaussian (e.g., likelihood function for strike at an early stage of the La Habra earthquake, Fig. 5), only the value with maximum likelihood is shown. Figure 5 displays three randomly picked screenshots for each event to illustrate the temporal rupture evolution.

The off-line-predicted rupture parameters for the La Habra and South Napa earthquakes (Figs. 4 and 5) are quite similar to the real-time results (Fig. 2). Again, because of the sparseness of seismic instrumentation around the South Napa earthquake, uncertainties in the *FinDer* output are quite large.

The **M** 7.2 El Mayor–Cucapah earthquake on 4 April 2010 occurred in northern Baja California in an area with a high level of historical seismicity, around 60 km south of the Mexico–United States border (Hauksson *et al.*, 2011). The event exhibited complex faulting, possibly starting as a smaller **M** ∼ 6 normal-faulting earthquake, followed ∼15 s later by the normal or strike-slip faulting mainshock with $\Theta_{obs} = 132°$ (Wei *et al.*, 2011). The aftershock zone extends from the southern end of the Elsinore fault zone in southern California almost to the northern tip of the Gulf of California, over a length of $L_{obs} = 120$ km (Hauksson *et al.*, 2011).

At the time of the El Mayor–Cucapah earthquake, *ShakeAlert* did not yet exist. However, all three point-source algorithms that are contributing to the current system were running in real-time test mode: τ_c–P_d *Onsite* detected the event within 16 s, *Virtual Seismologist* within 28 s of origin. Both algorithms estimated the event as **M** ∼ 6, that is, they were obviously confused by the smaller foreshock and underestimated the size of the mainshock. *ElarmS* did not process this event, because it was outside of the CISN network. At the time of the El Mayor–Cucapah earthquake, none of the Centro de Investigación Científica y de Educació n Superior de Ensenada (CICESE) Baja California, Mexico Seismic Network (Red Sismica del Noroeste de Mexico [RESNOM]) stations deployed in northern Mexico was streaming real-time waveform data to CISN, so only Californian sta-

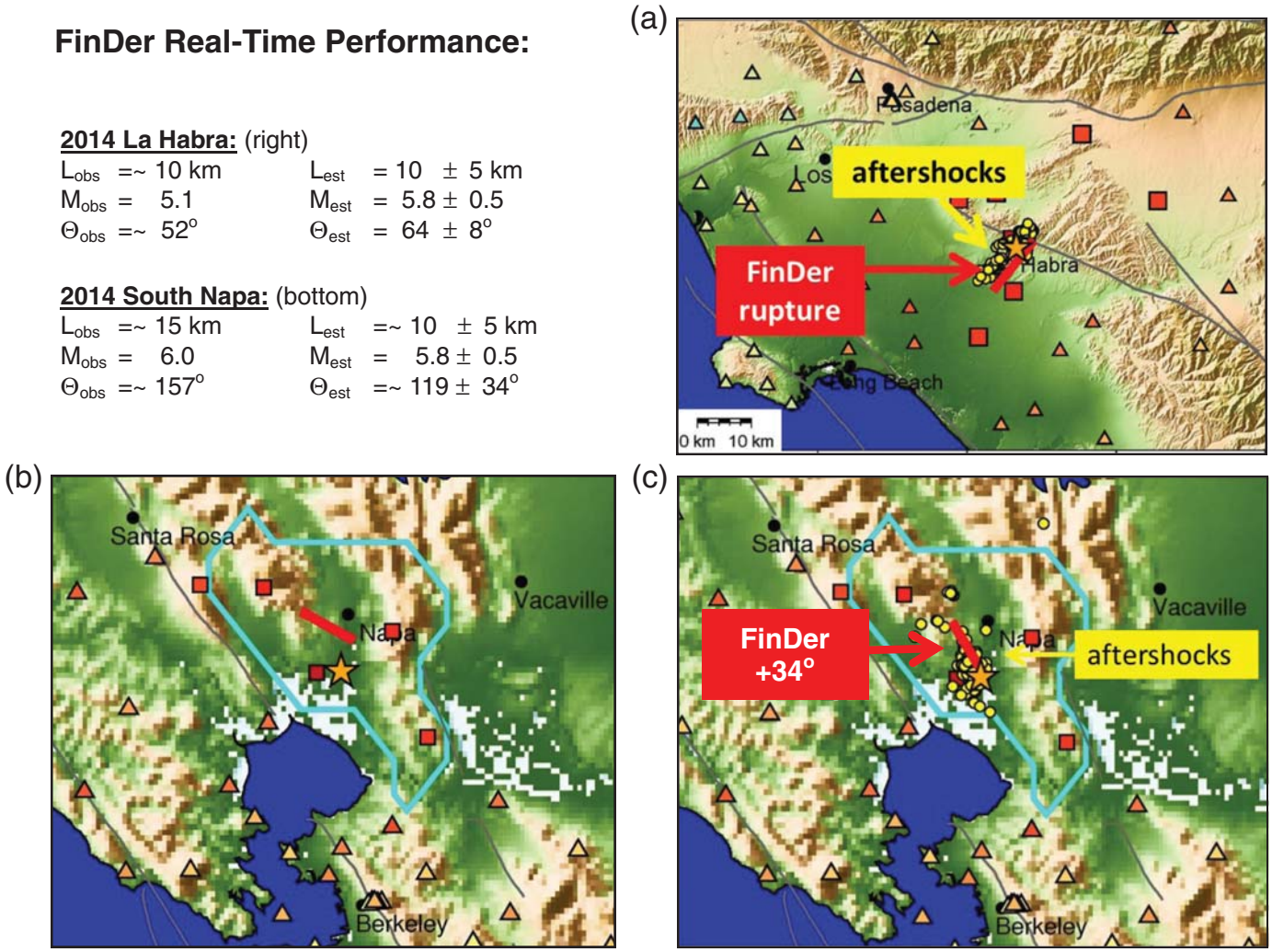

▲ **Figure 3.** *FinDer* real-time output for the 2014 (a) **M** 5.1 La Habra and (b, c) **M** 6.0 South Napa earthquakes. First reports were available within 11.5 s (La Habra) and 16 s (South Napa) of event origin. Maps and data block show results from the final *FinDer* report. Triangles and squares, respectively, mark the California Integrated Seismic Network (CISN) strong-motion stations at which peak ground accelerations are $(PGA)_{obs} < 70$ cm/s^2 and $PGA_{obs} \geq 70$ cm/s^2. (b) Because of sparse instrumentation, the strike Θ of the Napa earthquake is not well constrained. Though the final strike estimate is off by ~40°, the Global Centroid Moment Tensor (CMT) solution ($\Theta_{obs} = 157°$) is within the *FinDer* real-time-estimated uncertainty range. Solutions in (b) and (c) are equivalent, because they are producing almost the same misfit between observed and predicted high-frequency ground motions. For both earthquakes, there is an excellent agreement between the *FinDer*-predicted line source (red), CMT solutions (Table 2), and distribution of aftershocks (yellow circles).

tions were available in real time. Only recently, eight CICESE stations were added to the CISN live streams and are now being processed routinely by *ShakeAlert*.

For our *FinDer* off-line-test, we complemented the CISN waveform dataset with the data from eight CICESE stations (Fig. 5; see Data and Resources). Although the near-source station coverage is still quite poor, both the length and strike of the northwestern part of the bilateral rupture can be well recovered (Figs. 2, 4, and 5). The rupture centroid appears to be slightly shifted toward the east but is within the uncertainty range of our current map resolution (5 km). The final rupture length is estimated as 70 km, which corresponds to **M** ~ 7.1 (Wells and Coppersmith, 1994) and is thus in good agreement with the observed moment magnitude. The output of *FinDer* seems to be largely unaffected by the smaller **M** ~ 6 foreshock and inherent complexities of this event.

The last earthquake that we will analyze here is the 2011 **M** 9.0 Tohoku-Oki (Japan) megathrust earthquake, which caused tremendous numbers of casualties and damage in Iwate, Miyagi, and Fukushima, particularly from a Pacific-wide tsunami. Simons *et al.* (2011) estimate that peak displacements of around 60 m occurred along the central section of the fault plane (Fig. 2). Kinematic inversions by Minson, Simons, *et al.* (2014) suggest that the rupture propagated with a low average velocity of about 1.2 km/s and that most of the rupture occurred within ~120–125 s.

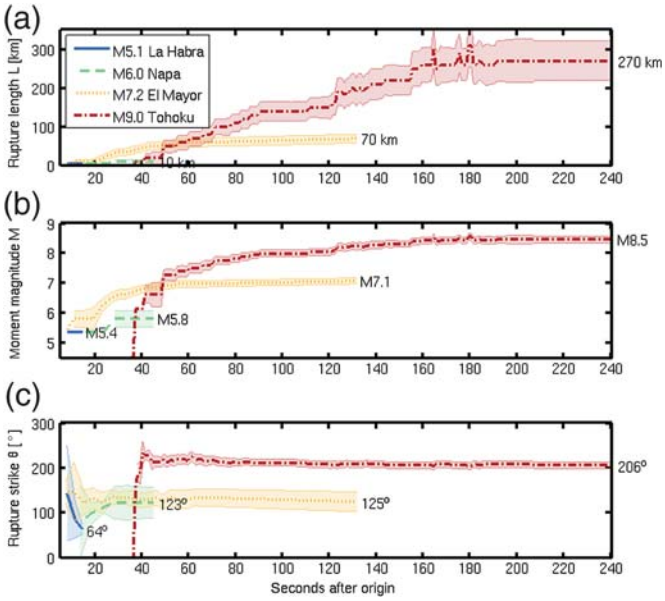

▲ **Figure 4.** Temporal evolution of *FinDer*-predicted (a) rupture length *L*, (b) moment magnitude **M**, and (c) rupture strike Θ in off-line test runs using archived waveforms of the **M** 5.1 La Habra, **M** 6.0 South Napa, **M** 7.2 El Mayor–Cucapah, and **M** 9.0 Tohoku-Oki earthquakes (compare with Table 2). The shaded areas show 68% confidence intervals estimated from the likelihood functions. Snapshots are shown in Figure 5.

The EEW system operated by the Japanese Meteorological Agency (JMA; Hoshiba *et al.*, 2008) detected the event within ~25 s from event origin and successfully released a warning to the Japanese public. However, because the event magnitude was underestimated and source finiteness not considered, ground motions were largely underestimated, in particular in the Kanto district (Hoshiba *et al.*, 2011).

For our *FinDer* off-line test, we use strong-motion records of the Tohoku-Oki earthquake from 273 K-NET stations operated by the Japanese National Research Institute for Earth Science and Disaster Prevention (NIED; see Data and Resources). Because the seismic observations in our test are limited to onshore stations and are thus restricted to one side of the fault rupture (Fig. 5, bottom), we use our generic asymmetric template set (Fig. 1, right; Table 1). Constrained by the geometry of the Japan trench, we assume a lower and upper strike limit of 90° and 270°, respectively, that is a westward-orientated dip.

In general, *FinDer* results (Fig. 4) become available a bit later than in the JMA EEW system, mainly because we are considering K-NET stations only. Although the strike stays quite stable after 40 s, we observe a steady increase in rupture length (and thus magnitude) up to 270 km and **M** 8.5 within 160 s after rupture nucleation, which seems to be consistent with the source time function of the Tohoku-Oki earthquake (Minson, Simons, *et al.*, 2014). The rupture centroid, in general, is not well constrained for a low-dipping fault plane and is also affected by boundary conditions of the ground-motion interpolation caused by the one-sided station coverage. In the test shown in this article (Figs 4 and 5), we set image pixels at ≥ 10 km distance from the closest recording station to 0 to avoid artifacts from interpolation.

Using KiK-net stations in addition to K-NET stations has no significant impact on the *FinDer* performance. The apparent underestimation of rupture length ($L_{est} \approx 270$ km) is thus likely not due to station density, but mainly a result of using the GMPE by Si and Midorikawa (2000), which predicts quite large shaking far from the fault rupture. The *FinDer* solution is consistent with the observed ground-motion distribution and applied GMPE and, as such, is useful to predict future shaking at larger distances (using the same GMPE) as needed for EEW. For illustration, in Figure 6 we compare the temporal evolution of observed and predicted JMA intensities in Tokyo. The predicted values are computed from Midorikawa *et al.* (1999) and Si and Midorikawa (2000) using the distance to the *FinDer*-estimated finite-fault rupture. Lead times between predicted and observed intensity levels range up to 50 s.

Minson, Simons, *et al.* (2014) report that high-frequency motions in the Tohoku-Oki earthquake were predominantly radiated down-dip of the regions of largest fault slip, particularly south of Sendai. Because *FinDer* uses high-frequency motions to determine rupture dimensions, the lack of correlation between high- and low-frequency motions could potentially lead to an underestimation of rupture dimensions, too.

DISCUSSION

Aside from the estimated finite-fault rupture parameters, there are two further aspects that make *FinDer* distinct from other current EEW algorithms: (1) *FinDer* searches for suspicious ground-motion patterns by looking at observed ground-motion images as a whole. This means that the *FinDer* output is a true network solution that combines spatially distributed observations instead of averaging over them, and (2) *FinDer* can be operated in two modes: either as a complete stand-alone algorithm or by being triggered by another algorithm or module. In the first mode, *FinDer* scans real-time ground-motion amplitudes continuously for suspicious patterns, and whenever the correlation between the observed ground motions (in space and time) and the theoretical templates exceeds some predefined threshold (e.g., $R > 0.9$), it starts sending out reports with the computed source parameters, completely autonomous from any other (point-source) algorithm. In the second mode, *FinDer* requires a trigger from another algorithm to get started and can then be used to verify a potential detection and compute source parameters.

Traditional picker and (pick-to-event) associators are designed to provide high-fidelity locations. If there is a complex sequence, such as a seismic swarm or increased aftershock activity, traditional associators can become confused, because it becomes unclear which picks go with which event. This was, for instance, the case during the intense aftershock activity following the **M** 9.0 Tohoku-Oki (Japan) earthquake, causing numerous false and missed alerts in the JMA EEW system (Hoshiba *et al.*, 2011). In EEW, we do not really care about

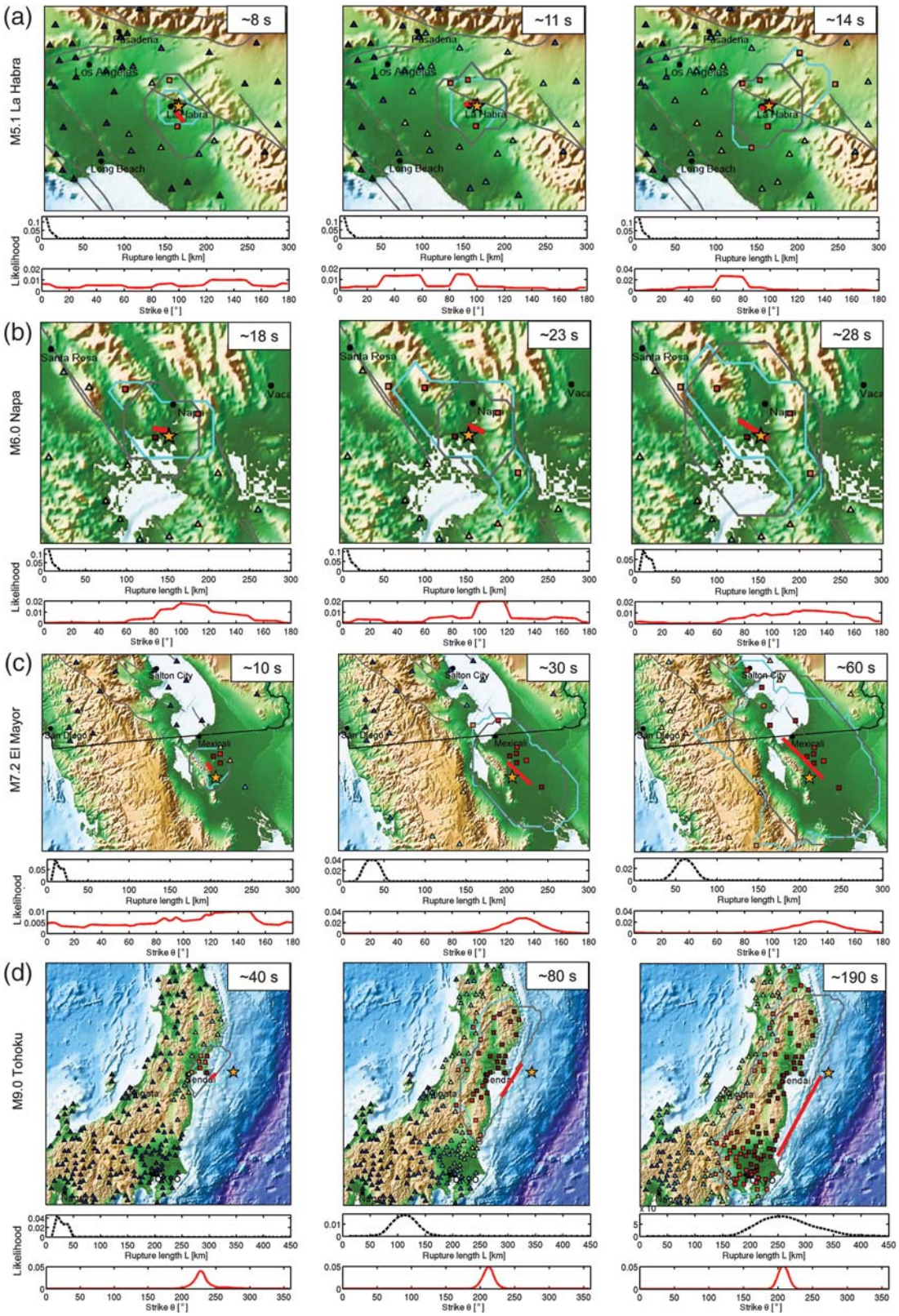

▲ **Figure 5.** Three randomly chosen times after nucleation taken during off-line test runs of *FinDer* for the (a) **M** 5.1 La Habra, (b) **M** 6.0 South Napa, (c) **M** 7.2 El Mayor–Cucapah, and (d) **M** 9.0 Tohoku-Oki earthquakes (compare with Fig. 2). The red lines show *FinDer*-estimated ruptures; near-source ($PGA_{obs} \geq 70$ cm/s^2) and far-source ($PGA_{obs} < 70$ cm/s^2) classified stations are shown by squares and triangles. Templates, which best fit near-source areas (cyan), are shown in gray. The likelihood functions quantifying reliability of estimated rupture length L and strike Θ are shown below each map.

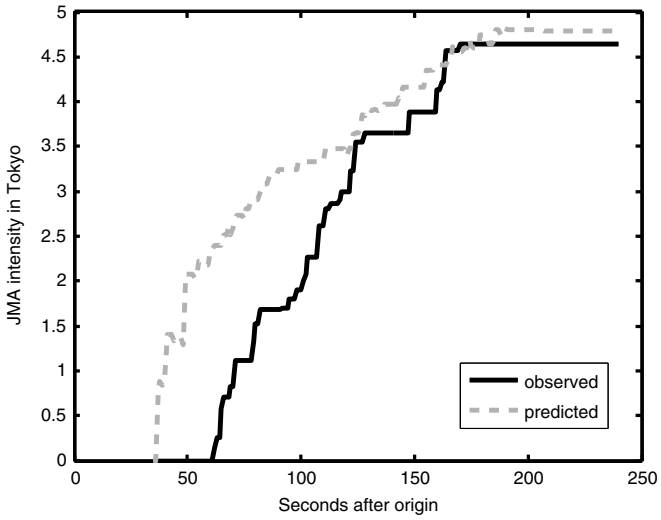

▲ **Figure 6.** Temporal evolution of observed and *FinDer*-predicted Japanese Meteorological Agency (JMA) intensity in Tokyo during the 2011 **M** 9.0 Tohoku-Oki earthquake.

these details, we just want to know the general time and place where the shaking originates. *FinDer* is therefore a simpler and more robust approach to association. These characteristics make *FinDer* likely also well suited for applications in highly noisy environments, as is typically observed in dense low-cost seismic and geodetic sensor networks, such as QuakeCatcher (Cochran *et al.*, 2009), the Community Seismic Network (Clayton *et al.*, 2011), or future crowd-sourced networks based on consumer smart devices (e.g., Minson *et al.*, 2015).

It is important to point out that the *FinDer*-estimated line sources depend on the GMPE used for template generation. Usually, *FinDer* results agree well with the observed fault ruptures; however, there is a chance that source dimensions are under- or overestimated (as could be seen in the case of the Tohoku-Oki earthquake; Figs. 4 and 5). Still, at any given time after rupture nucleation, the solution is consistent with the current spatial seismic ground-motion observations and the applied GMPE, and this is exactly what is needed for EEW (Fig. 6). To minimize the effects of shortcomings in the GMPEs on the *FinDer* result, we build our templates from ground-motion thresholds rather than complete GMPEs. The resulting binary images and templates are also less affected by uncertainties caused by the spatial interpolation of ground-motion amplitudes, particularly in sparsely instrumented regions.

To account for increasing uncertainties in spatially interpolated ground-motion values with increasing distances from the recording stations, we recently explored the usefulness of down-weighting image pixels that are far from observational sites, similar to what is done in the USGS *ShakeMaps* (Worden *et al.*, 2010). However, we found that for large *gm_thresholds* and application to dense station networks as in California, the effect of down-weighting is quite negligible. However, for subduction-zone events with one-sided station coverage, the benefit of down-weighting becomes more important. Böse *et al.* (2012) found that consideration of site effects of seismic ground motions has no significant impact on the *FinDer* solution.

It is also important to keep in mind that *FinDer* does not predict the future evolution of the fault rupture. Still, *FinDer*-estimated rupture dimensions allow prediction of future shaking at larger distances from the fault (as needed for EEW), which are more accurate for large earthquakes compared with what a point-source algorithm can achieve, because rupture-to-site distances can be taken into account. An instructive example is given by the **M** 7.8 ShakeOut scenario earthquake (Graves *et al.*, 2008) with a 300-km-long fault rupture along the SAF, starting at Bombay Beach and heading toward LA. Using a point-source approximation of the earthquake, shaking intensities in LA are predicted as light to moderate (modified Mercalli intensity [MMI] IV–V), whereas shaking in LA predicted with the *FinDer* finite-fault solution is severe (MMI VIII; Böse *et al.*, 2014). This value is much more consistent with seismic ground-motion simulations by Graves *et al.* (2008), which predict severe to violent shaking (MMI VIII–IX). In a big (finite-source) earthquake, much larger areas are affected by damaging ground-shaking compared with a small-to-moderate event; thus, many more people could benefit from EEW with warning times of several tens of seconds (Heaton, 1985).

Although *FinDer* itself does not provide predictions of future rupture, its output can be used for recognition of the fault along which rupture is occurring. This information, along with observed slip amplitudes and known fault characteristics, has potential to provide estimates of future rupture evolution (Böse and Heaton, 2010). Also, as demonstrated by Böse *et al.* (2014) using the Southern California Earthquake Center CyberShake dataset, the *FinDer* output can help to determine the direction in which a fault rupture is propagating and thus can help to enhance ground-motion predictions with consideration of directivity effects.

Last but not least, *FinDer* source dimensions and uncertainty estimates can constrain Global Positioning System (GPS)-based inversions of fault slip and magnitudes without saturation in large earthquakes. With the development of the *FinDer-GPSlip* and *FinDer-BEFORES* algorithms, Böse, Heaton, and Hudnut (2013) and Minson, Böse, *et al.* (2014) provide the first seismic-geodetic approaches to EEW that are consistent with both seismic and geodetic observations at any time after rupture nucleation. Traditionally, finite-fault-slip models are inverted for a known fixed-fault geometry. In an EEW setting, however, rupture geometry is unknown *a priori*, and thus, it becomes necessary to simultaneously solve for the fault geometry and slip, which is a nonlinear and computationally expensive inverse problem (Minson, Murray, *et al.*, 2014). Using both seismic and geodetic real-time observations helps constrain both source geometry and slip and can replace simplified assumptions such as of San Andreas parallel rupture strike, which is typical in GPS inversions (e.g., Grapenthin *et al.*, 2014).

CONCLUSIONS AND OUTLOOK

Finite-fault rupture extent and azimuth are crucial for accurately predicting seismic ground motions in large earthquakes with moment magnitudes $\mathbf{M} \geq 6.0$ where source finiteness, rupture-to-site distances, and rupture directivity control ground shaking. Thus, detecting and modeling finite-fault ruptures in real time are essential to EEW and rapid emergency response. Following a period of extensive real-time and off-line testing, the finite-fault rupture detector algorithm, *FinDer* (Böse *et al.*, 2012), was recently successfully integrated in the California-wide *ShakeAlert* EEW demonstration system. Since April 2015, *FinDer* has been actively contributing to real-time *ShakeAlert* reports automatically sent to several hundreds of test users in California, thus complementing the three previous point-source algorithms (τ_c–P_d *Onsite*, *ElarmS*, and *Virtual Seismologist*) and improving *ShakeAlert* performance during large earthquakes.

Currently, *FinDer* is operated as a MATLAB stand-alone code with a C++ waveform-processing module installed at three CISN datacenters (Caltech/USGS-Pasadena, University of California–Berkeley, and USGS-Menlo Park) and is continuously scanning real-time waveform data streams from around 420 strong-motion stations in California for PGA patterns indicative of earthquakes. In a joint effort of USGS-Menlo Park, ETH Zurich, and Caltech, we have recently started to translate the current *FinDer* code to C++. The goal is to obtain a faster and more flexible implementation that allows easier maintenance and better integration into various seismic processing systems, including *EarthWorm/AQMS* (as currently used in *ShakeAlert*) and *SeisComp3* (as currently dominantly used in Europe; Olivieri and Clinton, 2012). The new C++ code will benefit from existing and widely tested free software libraries for computer vision (*Open Source Computer Vision*; http://opencv.org, last accessed September 2015) and geographic mapping (*Generic Mapping Tools*; Wessel *et al.*, 2013).

During the next two years, we plan to increase the robustness of the current code and develop the second-generation *FinDer 2* algorithm with important new features: the current *FinDer* code supports utilization of a single ground-motion threshold only, which in the current *ShakeAlert* installation is set to 70 cm/s^2. This value is usually exceeded only in moderate-to-large-magnitude earthquakes, for instance within 20 km from the fault rupture for $\mathbf{M} \sim 6.0$ or within 40 km for $\mathbf{M} \sim 7.0$ (Cua and Heaton, 2009). A high threshold provides stable detection of large events at the cost of reduced detection speed and missed detections of smaller earthquakes.

FinDer 2 will combine multiple ground-motion thresholds: starting with small values that are typically observed in small earthquakes or shortly after rupture nucleation, *FinDer 2* will progressively increase these thresholds to allow detecting earthquakes with $\mathbf{M} > 3.5$ with a gradual refinement of finite-fault parameter estimates in large events. This refinement will also benefit from the new error estimates in *FinDer* as described in this article.

DATA AND RESOURCES

Seismic waveforms used in this study were downloaded from California Integrated Seismic Network (CISN) (http://www.cisn.org, last accessed July 2015), NIED (http://www.kik.bosai.go.jp, last accessed July 2015), and Red Sismica del Noroeste de Mexico (RESNOM)/Centro de Investigación Científica y de Educació n Superior de Ensenada (CICESE) (http://resnom.cicese.mx/sitio/, last accessed July 2015). A description of the *ShakeAlert* performance during the 2014 La Habra earthquake was obtained from http://earthquake.usgs.gov/earthquakes/eventpage/ci15481673#general_summary (last accessed August 2015). The Global Centroid Moment Tensor (CMT) project database was searched using www.globalcmt.org/CMTsearch.html (last accessed August 2015). USGS *ShakeMaps* in Figure 2 were downloaded from http://earthquake.usgs.gov/earthquakes/shakemap/ (last accessed August 2015). Maps in Figures 3 and 5 were made using *Generic Mapping Tools* (GMT; Wessel *et al.*, 2013).

ACKNOWLEDGMENTS

The authors would like to thank Sarah Minson, Deborah Smith, Egill Hauksson, Men-Andrien Meier, Yannik Behr, Carlo Cauzzi, John Clinton, and two anonymous reviewers and editors for discussions on *FinDer* and/or proofreading and reviewing of the manuscript. This work was funded by the U.S. Geological Survey and the Gordon and Betty Moore Foundation.

REFERENCES

Allen, R. M. (2007). The ElarmS earthquake early warning methodology and its application across California, in *Earthquake Early Warning Systems*, P. Gasparini, G. Manfredi, and J. Zschau (Editors), Springer, Berlin, Germany, 21–44, ISBN-13 978-3-540-72240-3.

Allen, R. M., P. Gasparini, O. Kamigaichi, and M. Böse (2009). The status of earthquake warning around the world: An introductory overview, *Seismol. Res. Lett.* **80,** no. 5, 682–693.

Behr, Y., J. F. Clinton, P. Kästli, C. Cauzzi, R. Racine, and M.-A. Meier (2015). Anatomy of an earthquake early warning (EEW) alert: Predicting time delays for an end-to-end EEW system, *Seismol. Res. Lett.* **86,** no. 3, 830–840, doi: 10.1785/0220140179.

Blaser, L., F. Krüger, M. Ohrnberger, and F. Scherbaum (2010). Scaling relations of earthquake source parameter estimates with special focus on subduction environment, *Bull. Seismol. Soc. Am.* **100,** 2914–2926.

Böse, M., and T. H. Heaton (2010). Probabilistic prediction of rupture length, slip and seismic ground motions for an ongoing rupture: Implications for early warning for large earthquakes, *Geophys. J. Int.* **183,** no. 2, 1014–1030, doi: 10.1111/j.1365-246X.2010.04774.x.

Böse, M., R. Allen, H. Brown, G. Cua, M. Fischer, E. Hauksson, T. Heaton, M. Hellweg, M. Liukis, D. Neuhauser, *et al.* (2013). CISN ShakeAlert—An earthquake early warning demonstration system for California, in *Early Warning for Geological Disasters—Scientific Methods and Current Practice*, F. Wenzel and J. Zschau (Editors), Springer, Berlin, Germany, ISBN: 978-3-642-12232-3.

Böse, M., R. Graves, D. Gill, S. Callaghan, and P. Maechling (2014). CyberShake-derived ground-motion prediction models for the Los

Angeles region with application to earthquake early warning, *Geophys. J. Int.* **198,** no. 3, 1438–1457, doi: 10.1093/gji/ggu198.

Böse, M., E. Hauksson, K. Solanki, H. Kanamori, and T. H. Heaton (2009). Real-time testing of the on-site warning algorithm in southern California and its performance during the July 29 2008 M_w 5.4 Chino Hills earthquake, *Geophys. Res. Lett.* **36,** L00B03, doi: 10.1029/2008GL036366.

Böse, M., E. Hauksson, K. Solanki, H. Kanamori, Y.-M. Wu, and T. H. Heaton (2009). A new trigger criterion for improved real-time performance of on-site earthquake early warning in southern California, *Bull. Seismol. Soc. Am.* **99,** no. 2-A, 897–905, doi: 10.1785/0120080034.

Böse, M., T. H. Heaton, and E. Hauksson (2012). Real-time finite fault rupture detector (FinDer) for large earthquakes, *Geophys. J. Int.* **191,** no. 2, 803–812, doi: 10.1111/j.1365-246X.2012.05657.x.

Böse, M., T. Heaton, and K. Hudnut (2013). Combining real-time seismic and GPS data for earthquake early warning, *AGU Fall Meeting 2013*, San Francisco, California, 9–13 December, Abstract Number G51B-05.

Clayton, R. W., T. Heaton, M. Chandy, A. Krause, M. Kohler, J. Bunn, R. Guy, M. Olson, M. Faulkner, M.-H. Cheng, *et al.* (2011). Community seismic network, *Ann. Geophys.* **54,** no. 6, doi: 10.4401/ag-5269.

Cochran, E. S., J. F. Lawrence, C. Christensen, and R. S. Jakka (2009). The Quake-Catcher network: Citizen science expanding seismic horizons, *Seismol. Res. Lett.* **80,** 26–30.

Cua, G., and T. H. Heaton (2009). *Characterizing Average Properties of Southern California Ground Motion Amplitudes and Envelopes*, Earthquake Engineering Research Laboratory, Pasadena, California, http://resolver.caltech.edu/CaltechEERL:EERL-2009-05 (last accessed September 2015).

Cua, G. B., M. Fischer, T. H. Heaton, and S. Wiemer (2009). Real-time performance of the virtual seismologist earthquake early warning algorithm in southern California, *Seismol. Res. Lett.* **80,** no. 5, 740–747, doi: 10.1785/gssrl.80.5.740.

Erdik, M., Y. Fahjan, O. Ozel, H. Alcik, A. Mert, and M. Gul (2003). Istanbul earthquake rapid response and the early warning system, *Bull. Earthq. Eng.* **1,** 157–163.

Espinosa-Aranda, J., A. Jimenez, G. Ibarrola, F. Alcantar, A. Aguilar, M. Inostroza, and S. Maldonado (1995). Mexico City seismic alert system, *Seismol. Res. Lett.* **66,** no. 6, 42–53.

Gonzales, R. C., R. F. Woods, and S. L. Eddins (2004). *Digital Image Processing Using MATLAB*, Pearson Prentice Hall, Upper Saddle River, New Jersey.

Grapenthin, R., I. Johanson, and R. M. Allen (2014). The 2014 M_w 6.0 Napa earthquake, California: Observations from real-time GPS-enhanced earthquake early warning, *Geophys. Res. Lett.* **41,** 8269–8276, doi: 10.1002/2014GL061923.

Graves, R. W., B. T. Aagaard, K. W. Hudnut, L. M. Star, J. P. Stewart, and T. H. Jordan (2008). Broadband simulations for M_w 7.8 southern San Andreas earthquakes: Ground motion sensitivity to rupture speed, *Geophys. Res. Lett.* **35,** L22302, doi: 10.1029/2008GL035750.

Hauksson, E., J. Stock, K. Hutton, W. Yang, J. A. Vidal-Villegas, and H. Kanamori (2011). The 2010 M_w 7.2 El Mayor–Cucapah earthquake sequence, Baja California, Mexico and southernmost California, USA: Active seismotectonics along the Mexican Pacific margin, *Pure Appl. Geophys.* **168,** no. 8/9, 1255–1277.

Heaton, T. H. (1985). A model for a seismic computerized alert network, *Science* **228,** 987–990.

Hoshiba, M., K. Iwakiri, N. Hayashimoto, T. Shimoyama, K. Hirano, Y. Yamada, Y. Ishigaki, and H. Kikuta (2011). Outline of the 2011 Off the Pacific Coast of Tohoku earthquake (M_w 9.0)—Earthquake early warning and observed seismic intensity, *Earth Planets Space* **63,** 547–551.

Hoshiba, M., O. Kamigaichi, M. Saito, S. Tsukada, and N. Hamada (2008). Earthquake early warning starts nationwide in Japan, *Eos Trans. AGU* **89,** 73–74.

Hsiao, N.-C., Y.-M. Wu, L. Zhao, D.-Y. Chen, W.-T. Huang, K.-H. Kuo, T.-C. Shin, and P.-L. Leu (2011). A new prototype system for earthquake early warning in Taiwan, *Soil Dynam. Earthquake. Eng.* **31,** no. 2, 201–208, doi: 10.1016/j.soildyn.2010.01.008.

Kuyuk, S., R. M. Allen, H. Brown, M. Hellweg, I. Henson, and D. Neuhauser (2014). Designing a network-based earthquake early warning algorithm for California: ElarmS-2, *Bull. Seismol. Soc. Am.* **104,** no. 1, 162–173, doi: 10.1785/0120130146.

Lagarias, J. C., J. A. Reeds, M. H. Wright, and P. E. Wright (1998). Convergence properties of the Nelder–Mead simplex method in low dimensions, *SIAM J. Optim.* **9,** no. 1, 112–147.

Lay, T., C. J. Ammon, H. Kanamori, L. Xue, and M. J. Kim (2011). Possible large near-trench slip during the 2011 M_w 9.0 Off the Pacific Coast of Tohoku earthquake, *Earth Planets Space* **63,** 687–692.

Mai, P. M., and K. K. S. Thingbaijam (2014). SRCMOD: An online database of finite-fault rupture model, *Seismol. Res. Lett.* **85,** no. 6, 1348–1357, doi: 10.1785/0220140077.

Mărmureanu, A., C. Ionescu, and C. O. Cioflan (2011). Advanced real-time acquisition of the Vrancea earthquake early warning system, *Soil Dynam. Earthq. Eng.* **31,** no. 2, 163–169, doi: 10.1016/j.soildyn.2010.10.002.

Midorikawa, S., K. Fujimoto, and I. Muramatsu (1999). Correlation of new JMA instrumental seismic intensity with former JMA seismic intensity and ground motion parameters, *J. Soc. Saf. Sci.* **1,** 51–56.

Minson, S., M. Böse, C. Felizardo, T. H. Heaton, and E. Hauksson (2014). Joint seismic-geodetic real-time finite fault models for earthquake early warning, *American Geophysical Union, Fall Meeting 2014*, San Francisco, California, 15–19 December 2014, abstract #S32C-04.

Minson, S. E., B. A. Brooks, C. L. Glennie, J. R. Murray, J. O. Langbein, S. E. Owen, T. H. Heaton, R. A. Iannucci, and D. L. Hauser (2015). Crowd sourced earthquake early warning, *Sci. Adv.* **1,** no. 3, e1500036, doi: 10.1126/sciadv.1500036.

Minson, S. E., J. R. Murray, J. O. Langbein, and J. S. Gomberg (2014). Real-time inversion for finite-fault slip models and rupture geometry based on high-rate GPS data, *J. Geophys. Res.* **119,** 3201–3231, doi: 10.1002/2013JB010622.

Minson, S. E., M. Simons, J. L. Beck, F. Ortega, J. Jiang, S. E. Owen, A. W. Moore, A. Inbal, and A. Sladen (2014). A Bayesian approach to finite fault earthquake modeling II: Application to the Great 2011 Tohoku-Oki earthquake, *Geophys. J. Int.* **198,** no. 2, 922–940, doi: 10.1093/gji/ggu170.

Olivieri, M., and J. Clinton (2012). An almost fair comparison between Earthworm and SeisComp3, *Seismol. Res. Lett.* **83,** no. 4, 720–727, doi: 10.1785/0220110111.

Peng, H., Z. Wu, Y.-M. Wu, S. Yu, D. Zhang, and W. Huang (2011). Developing a prototype earthquake early warning system in the Beijing capital region, *Seismol. Res. Lett.* **82,** no. 3, 394–403, doi: 10.1785/gssrl.82.3.394.

Satriano, C., L. Elia, C. Martino, M. Lancieri, A. Zollo, and G. Iannaccone (2011). PRESTo, the earthquake early warning system for southern Italy: Concepts, capabilities and future perspectives, *Soil Dynam. Earthq. Eng.* **31,** no. 2, 137–153, doi: 10.1016/j.soildyn.2010.06.008.

Si, H., and S. Midorikawa (2000). New attenuation relations for peak ground acceleration and velocity considering effects of fault type and site condition, *Proc. of 12th World Conf. on Earthquake Engineering*, Auckland, New Zealand, 30 January–4 February 2000, Paper Number 0532.

Simons, M., S. E. Minson, A. Sladen, F. Ortega, J. Jiang, S. E. Owen, L. Meng, J.-P. Ampuero, S. Wei, R. Chu, *et al.* (2011). The 2011 magnitude 9.0 Tohoku-Oki earthquake: Mosaicking the megathrust from seconds to centuries, *Science* **332,** no. 6036, 1421–1425, doi: 10.1126/science.1206731.

Spudich, P., and B. S. J. Chiou (2008). Directivity in NGA earthquake ground motions: Analysis using isochrone theory, *Earthq. Spectra* **24,** no. 1, 279–298, doi: 10.1193/1.2928225.

Yamada, M., T. Heaton, and J. Beck (2007). Real-time estimation of fault rupture extent using near-source versus far-source classification, *Bull. Seismol. Soc. Am.* **97,** no. 6, 1890–1910.

Wald, D., V. Quitoriano, T. Heaton, H. Kanamori, C. Scrivner, and C. Worden (1999). TriNet ShakeMaps: Rapid generation of instrumental ground motion and intensity maps for earthquakes in southern California, *Earthq. Spectra* **15,** 537–556.

Wei, S., E. Fielding, S. Leprince, A. Sladen, J. P. Avouac, D. Helmberger, E. Hauksson, R. Chu, M. Simons, K. Hudnut, *et al.* (2011). Superficial simplicity of the 2010 El Mayor–Cucapah earthquake of Baja California in Mexico, *Nat. Geosci.* **4,** 615–618, doi: 10.1038/ngeo1213.

Wells, D. L., and K. J. Coppersmith (1994). New empirical relationships among magnitude, rupture length, rupture width, rupture area, and surface displacement, *Bull. Seismol. Soc. Am.* **84,** 974–1002.

Wessel, P., W. H. F. Smith, R. Scharroo, J. F. Luis, and F. Wobbe (2013). Generic mapping tools: Improved version released, *Eos Trans. AGU* **94,** 409–410.

Worden, C. B., D. J. Wald, K. Lin, G. Cua, and D. Garcia (2010). A revised ground-motion and intensity interpolation scheme for ShakeMap, *Bull. Seismol. Soc. Am.* **100,** 3083–3096.

Wu, Y.-M., H. Kanamori, R. M. Allen, and E. Hauksson (2007). Determination of earthquake early warning parameters, τ_c and P_d, for southern California, *Geophys. J. Int.* **170,** 711–717, doi: 10.1111/j.1365-246X.2007.03430.x.

M. Böse
Swiss Federal Institute of Technology Zurich (ETHZ)
Geophysical Institute
Swiss Seismological Service
Sonneggstrasse 5
8092 Zürich, Switzerland
mboese@sed.ethz.ch

C. Felizardo
T. H. Heaton
California Institute of Technology (Caltech)
1200 E California Boulevard
Pasadena, California 91125 U.S.A.
claude@gps.caltech.edu
heaton@caltech.edu

Published Online 07 October 2015